Low Phase Noise Wide Tuning Range *N*-Push Cyclic-Coupled Ring Oscillators

Mohammed M. Abdul-Latif, *Student Member, IEEE*, and Edgar Sánchez-Sinencio, *Life Fellow, IEEE*

***Abstract*—Cyclic-coupled ring oscillators (CCRO) provide several unique features over regular ring oscillators such as availability of multiple sets of phase-shifted outputs and reduced phase noise. Furthermore, when combined with *N*-push frequency multiplication low phase noise, wide tuning ranges and millimeter-wave (mm-wave) frequencies can be realized. In this work, we propose two *N*-push CCROs fabricated in a 90 nm digital CMOS process. First, a wideband *N*-Push/*M*-Push CCRO is presented which achieves an output frequency range of 3.16–12.8 GHz using a unit cell ring oscillator operating at 1–2.56 GHz. The measured phase noise at 1 MHz offset is -103.4 dBc/Hz and -101.6 dBc/Hz at 3.16 GHz and 12.8 GHz, respectively. Second, an mm-wave *N*-Push CCRO is presented. It generates an output frequency of 13–25 GHz with a low phase noise performance of -95 dBc/Hz at 1 MHz offset over the output frequency range. The proposed oscillators achieve superior phase noise performance as well as competitive figure-of-merit compared with the state-of-the-art ring oscillators. In addition, the operation of the CCRO and its phase noise is analyzed. We confirm, analytically and experimentally, that the phase noise of an *M*-stage CCRO improves by 10log*M* over that of a single ring oscillator. We also show that the phase noise improvement bandwidth is a function of the coupling strength.**

***Index Terms*—Coupled oscillators, frequency multiplier, millimeter wave, N-push, ring oscillators, wideband.**

I. INTRODUCTION

OSCILLATORS are essential components in numerous circuits such as frequency synthesizers for wireless and wireline transceivers, clock generators for microprocessors and clock and data recovery systems. The high demand on data and bandwidth requires that these oscillators work at higher frequencies to process more data and provide more bandwidth. Higher data rates also require that oscillators have lower phase noise. In addition, oscillators are required to provide multi-phase clocks; for example in-phase and quadrature-phase clocks in fully integrated image reject receivers [1] or multi-phase clocks employed in high speed sampling in time-interleaved applications [2].

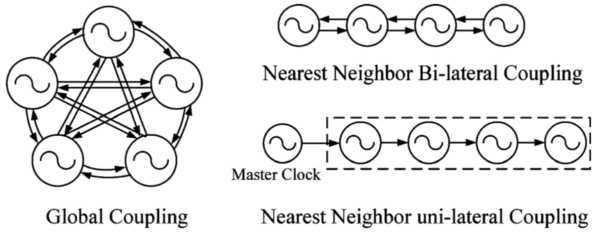

Fig. 1. Configurations of coupled oscillators [4].

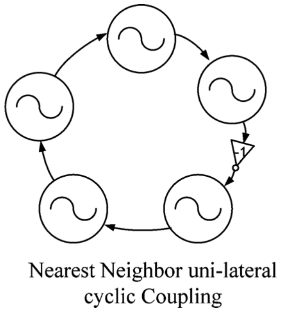

Fig. 2. Cyclic coupled oscillators [5]–[8].

Coupled oscillators have been used historically to provide multi-phase outputs for power combining and beam scanning applications [3]. They have the advantage of reduced phase noise: M coupled oscillators have M times less phase noise than a single oscillator (given the coupling network is reciprocal) [4]. However, for LC-tank coupled oscillators, the phase noise improvement is not $1/M$ because phase noise of the individual oscillators degrades due to de-tuning of the oscillator output frequency from the tank's resonance frequency [5], [6]. Moreover, the area penalty of using on-chip inductors limits the number of achievable phases and the narrowband characteristics of the LC-tanks limits wideband frequency operation. On the other hand, ring oscillators inherently provide multi-phase clocks as well as wide tuning ranges. In addition, they are compatible with the low cost digital CMOS processes and scale with technology promising higher operating frequencies for newer deep submicron technologies. However, their phase noise performance is inferior to LC oscillators.

In this work we propose to exploit the advantages of ring oscillators while improving their phase noise performance through the use of coupled oscillators. Fig. 1 shows different architectures of coupled oscillators reported in [4]. Fig. 2 shows a cyclic coupled oscillator structure where oscillators are placed in a ring structure with each oscillator injecting a scaled copy of its signal into the succeeding oscillator [5]–[8]. Cyclic coupled ring oscillators (CCROs) were reported in [9] to provide high resolution multi-phase outputs. Here we revisit the cyclic coupled ring oscillators and propose to use the different sets of phase-shifted

---

Manuscript received August 08, 2011; revised December 08, 2011; accepted February 14, 2012. Date of publication April 04, 2012; date of current version May 22, 2012. This paper was approved by Associate Editor Hooman Darabi. This work was supported in part by Texas Instruments Inc.

M. M. Abdul-Latif is with the Analog and Mixed Signal Center, Department of Electrical and Computer Engineering, Texas A&M University, College Station, TX 77843 USA (e-mail: mohdmohsen2002@gmail.com).

E. Sánchez-Sinencio is with the Analog and Mixed Signal Center, Department of Electrical and Computer Engineering, Texas A&M University, College Station, TX 77843 USA (e-mail: sanchez@ece.tamu.edu).

Color versions of one or more of the figures in this paper are available online at http://ieeexplore.ieee.org.

Digital Object Identifier 10.1109/JSSC.2012.2188564

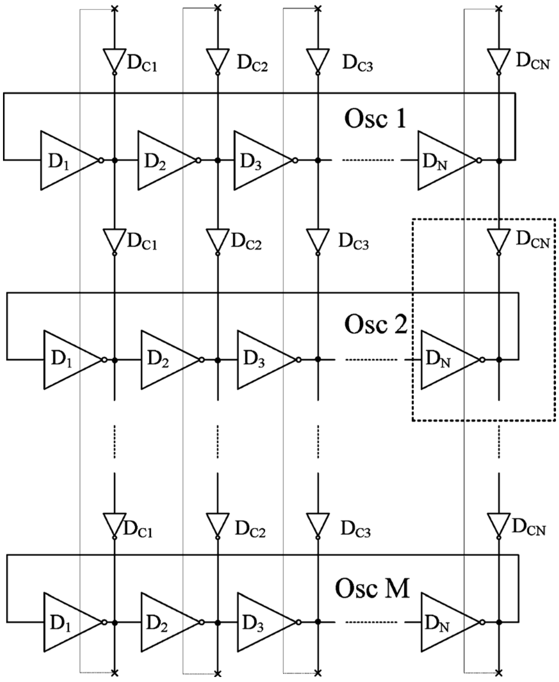

Fig. 3. Circuit diagram of the CCRO.

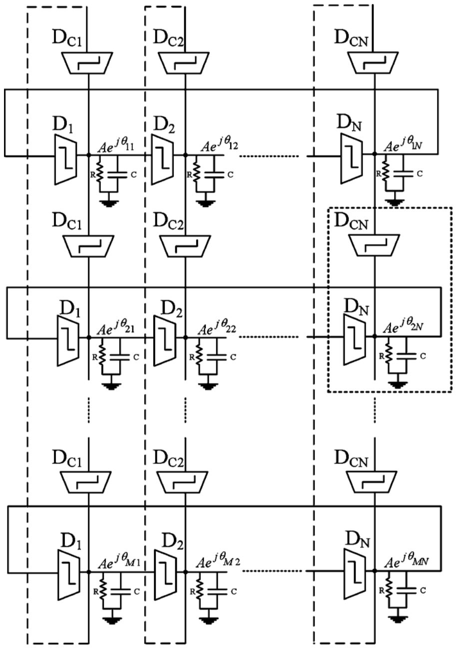

Fig. 4. Circuit model of the CCRO.

outputs in the implementation of N-Push frequency multiplication [10]. We show that the combined N-push CCRO architecture can provide wideband and mm-wave frequency outputs with low phase noise. First, we present a wideband oscillator based on this technique which can operate from 3.16–12.8 GHz using a ring oscillator core operating at 1–2.56 GHz by leveraging two sets of multi-phase outputs available from the CCRO [11]. Second, we use this architecture to design another N-Push CCRO operating from 13–25 GHz with a low phase noise performance. In addition, we analyze the CCRO, derive the different oscillation modes and their stability as well as derive the phase noise expression of an M-stage CCRO. We confirm analytically and experimentally that the phase noise for this cyclic coupled topology improves by M times over that of a single ring oscillator. We also show that the phase noise improvement bandwidth is proportional to the coupling strength.

The paper is organized as follows: Section II presents the architecture of the CCRO as well as the oscillation modes analysis, their stability, and phase noise analysis. Section III presents the designed N-Push CCRO structures and their advantages. Measurement results are presented in Section IV while the paper is concluded in Section V.

II. CYCLIC-COUPLED RING OSCILLATOR

A. Architecture

Fig. 3 shows a cyclic coupled ring oscillator which presents a special case of the oscillator array proposed in [9]. It is composed of M identical ring oscillators, each composed of N main delay cells $(D_1\text{-}D_N)$. Coupling delay cells $(D_{C1}\text{-}D_{\mathrm{CN}})$ inject a scaled version of each oscillator's current into the next oscillator stage. The transconductances of the coupling delay cells $(D_{C1}\text{-}D_{\mathrm{CN}})$ are k times smaller than those of the main delay cells $(D_1\text{-}D_N)$, where k is called the coupling factor and is less than unity. The M oscillators form a ring structure such that output of each stage feeds the next and the Mth stage feeds the first stage. In other words, each N-stage ring oscillator is injection-locked to the previous ring oscillator using progressive phase injection at every node. This multi-point injection keeps the phase balance between all the nodes [12]. This coupled oscillator structure can also be viewed as M horizontal oscillators (with N stages each: $D_1\text{-}D_N$) combined with N vertical oscillators (with M stages each: $D_{C1}\text{-}D_{\mathrm{CN}}$). The vertical oscillators are designed to be weaker than the horizontal ones by a factor of k. In this work, a single ended architecture is adopted so M and N must be odd numbers; however, the proposed methodology can be also applied to differential structures. The delay cells of the ring oscillator as well as the coupling cells are implemented as static CMOS inverters.

B. Analysis of CCRO

In this section we analyze the CCRO to determine its oscillation frequency and phase noise and compare it to a single-loop N-stage ring oscillator. We also determine the modes of oscillation and their stability. The analysis in [13] describes how to analyze a system of coupled oscillators to arrive at the different oscillation modes and determine their stability using Adler's equation for injection locking. However, the above work uses tuned LC oscillators and not ring oscillators and hence, cannot be directly applied to our CCRO. Here we follow an approach similar to that proposed in [6] and [12] while taking into consideration the cyclic nature of the architecture. We model the main delay cells and the coupling delay cells as ideal transconductors with an RC load representing the parallel combination of their output impedances, as shown in Fig. 4. This model works for both single ended and differential delay cells. In the case of inverter based transconductances, the generated current is out-of-phase with the input voltage. Fig. 5 indicates the current generated by the main delay cell's transconductance (I_{osc}) and that generated

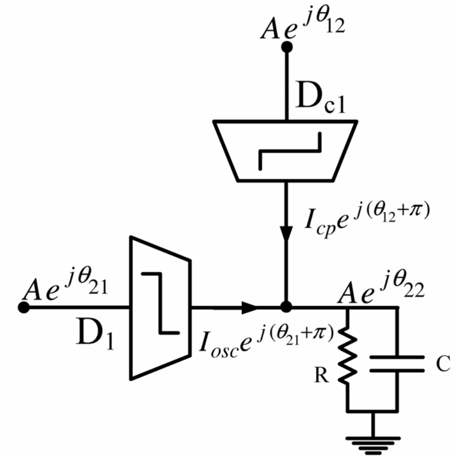

Fig. 5. Circuit model of node (2, 2) in the CCRO.

by the coupling delay cell's transconductance (I_{cp}). Both currents are injected and added into the output node. Writing KCL at the output node of the second delay cell of the second horizontal oscillator (node (2, 2)) yields

$$\frac{Ae^{j\theta_{22}}}{R}+C\frac{d(Ae^{j\theta_{22}})}{dt}=I_{osc}e^{j(\theta_{21}+\pi)}+I_{cp}e^{j(\theta_{12}+\pi)} \quad (1)$$

where A is the oscillation amplitude. Assuming hard limiting transconductors such that we can neglect dA/dt in (1) [12], we can solve the real and imaginary equations to obtain

$$\frac{d\theta_{22}}{dt}=\frac{1}{RC}\frac{I_{osc}\sin(\theta_{21}-\theta_{22})+I_{cp}\sin(\theta_{12}-\theta_{22})}{I_{osc}\cos(\theta_{21}-\theta_{22})+I_{cp}\cos(\theta_{12}-\theta_{22})}. \quad (2)$$

Generalizing to any arbitrary node (i,j) (i is the row index $(i=1\ldots N)$ and j is the column index $(j=1\ldots M)$) we have

$$\frac{d\theta_{ij}}{dt}=\frac{1}{RC}\frac{\sin(\theta_{i,j-1}-\theta_{ij})+k\sin(\theta_{i-1,j}-\theta_{ij})}{\cos(\theta_{i,j-1}-\theta_{ij})+k\cos(\theta_{i-1,j}-\theta_{ij})} \quad (3)$$

where $k=I_{cp}/I_{osc}$ is the coupling factor.

Defining the horizontal phase shift $\phi_j=\theta_{ij-1}-\theta_{ij}$ and the vertical phase shift $\psi_i=\theta_{i-1j}-\theta_{ij}$ for all values of i and j, and since $\theta_{ij}=\omega_{osc,i}t$ and $d\theta_{ij}/dt=\omega_{osc,i}$, then (3) can be rewritten as

$$\omega_{osc,i}=\frac{1}{RC}\frac{\sin(\phi_j)+k\sin(\psi_i)}{\cos(\phi_j)+k\cos(\psi_i)}. \quad (4)$$

If all oscillators lock to the same frequency, ω_0, and given the symmetry of the system, then $\phi_j=\phi_0$ for all j, $\psi_i=\psi_0$ for all i and the oscillation frequency of the CCRO is given as

$$\omega_0=\frac{1}{RC}\frac{\sin(\phi_0)+k\sin(\psi_0)}{\cos(\phi_0)+k\cos(\psi_0)}. \quad (5)$$

It should be noted that the oscillation frequency of a single unit oscillator can be obtained by putting $k=0$ in (5) to yield the same result as given in [12]

$$\omega_{osc,\text{single}}=\frac{\tan(\phi_0)}{RC}. \quad (6)$$

To obtain ϕ_0, we have to note that the horizontal ring oscillator is composed of N inverter stages (recalling that N is an odd number) and the total phase shift around the loop has to be $2n\pi$. However, since the injected current (I_{cp}) is much smaller than the oscillators intrinsic current (I_{osc}), then each main delay cell of the horizontal ring oscillator can only supply a phase shift which is less than $\pi/2$, i.e., $n=1$ only. Therefore, there is only one solution for ϕ_0 given by

$$\phi_0=\pi+\frac{\pi}{N}. \quad (7)$$

However, for the vertical ring oscillator, the number of inverter stages is M (where M is also an odd number) and the injected current (I_{osc}) is much larger than its intrinsic current (I_{cp}) and hence each coupling delay cell of the vertical ring oscillator can supply a phase shift which is larger then $\pi/2$, i.e., the phase shift around the loop can be multiples of 2π. Therefore, there might be more than one solution for ψ_0 given by

$$\begin{aligned} M\psi_0 &= 2n\pi \\ \psi_0 &= n\left(\frac{2\pi}{M}\right) \text{ where } \frac{M}{2}<n<M \end{aligned} \quad (8)$$

where different values of n correspond to different oscillation modes. For example, given $M=5$, $n=3$ or 4, i.e., $\psi_0=216^\circ$ or 288°.

To test the stability of these modes, we perform the perturbation analysis [6] shown in Appendix A. This analysis arrives at a matrix $[A]$, defined in (33)–(36) which defines the stability of the different oscillation modes. By finding the eigen values of the matrix $[A]$ for each available solution for ψ_0 we can determine the mode stability. Eigen values with a negative real part correspond to a stable mode. Since, the given equations are complicated to find an analytical solution, numerical methods were used for specific numbers of N and M. Results show that all modes calculated from (8) are stable modes. While [6] suggests that only the mode which undergoes the highest amplification grows faster and hence is sustained by the loop, it has been shown in [14] that startup non-linearity can make another mode prevail. However, it is noticed that all the stable modes have the same set of phase shifts. This means that anyone of those modes will be sufficient for the correct operation of our proposed application. More details are presented in Section III-B-1.

Next we carry out the graphical analysis of the CCRO model shown in Fig. 5 to determine the region of stable modes (allowable values of ψ_0). We take the voltage at node (2, 2), $Ae^{j\theta_{22}}$, as the reference so we can plot the phasor diagram of the currents as shown in Fig. 6(a) [6]. The total current entering the RC load, I_t, consists of two components: I_{osc} with a phase of $\phi_0'=\phi_0+\pi=\pi/N$ and I_{cp} with a phase of $\psi_0'=\psi_0+\pi$. Hence, I_t now lags the voltage by an angle α given by (9) which depends on ϕ_0, ψ_0 and k:

$$\tan(\alpha)=\frac{\sin(\phi_0)+k\sin(\psi_0)}{\cos(\phi_0)+k\cos(\psi_0)}. \quad (9)$$

The region of stable modes can be determined using the perturbation analysis outlined in [6] and is illustrated as the bolded area in Fig. 6(b) defined by $\alpha_{\min}$ to $\alpha_{\max}$. $\alpha_{\max}$ happens when I_t is tangent to the circle whose radius is I_{cp}. The angle $\psi'_{0,\max}$ in this case determines the upper boundary of the stable region of operation. In addition, since the delay cells are inverters $\pi<\psi_0<2\pi$, so $0<\psi_0'<\pi$ and hence $\psi'_{0,\min}=0$ determines the lower bound of the stable region. From the geometry

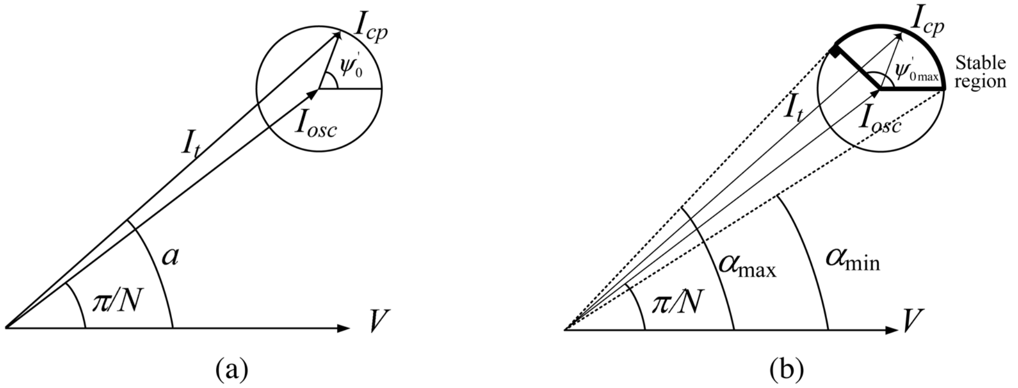

Fig. 6. (a) Phasor diagram of the currents of the CCRO. (b) Region of mode stability.

in Fig. 6(b) $\psi_{0,\max}'$ can be determined and used to identify the region of stable modes and is found to be

$$\psi_{0,\max}' = \frac{\pi}{N} - \cos^{-1}(k) + \pi. \tag{10}$$

Therefore, for a mode to be stable the value of the corresponding ψ_0 (calculated from (8)) should be less than $\psi_{0,\max} = \psi_{0,\max}' - \pi$ and larger than π. This is an easier way to determine mode stability.

Next, we determine the frequencies of the stable modes of the CCRO. We note that the oscillation frequency of the CCRO deviates from that of a single oscillator as indicated by (5) and (6). Hence, we can write the oscillation frequency of a CCRO as

$$\omega_0 = \omega_{osc,\text{single}} + \Delta\omega = \omega_p \tan(\alpha) \tag{11}$$

where $\omega_p = 1/RC$.

Using (9) and assuming $k \ll 1$, ω_0 can be derived to be

$$\omega_0 = \omega_{osc,\text{single}} + k\frac{\omega_0}{\frac{1}{2}\sin(2\phi_0)}\sin(\psi_0 - \phi_0). \tag{12}$$

Hence, the frequency of the stable mode depends on the corresponding ψ_0. In other words, if $\psi_0 < \phi_0$ then $\Delta\omega < 0$ and frequency decreases (α decreased), while if $\psi_0 > \phi_0$ then $\Delta\omega > 0$ and frequency increases (α increased) and if $\psi_0 = \phi_0$ then $\Delta\omega = 0$ and frequency is equal to that of a single ring oscillator. It should be noted that the shift in the oscillation frequency of the CCRO is scaled down by k indicating that frequency shift is much smaller than the oscillation frequency.

C. Phase Noise

One of the advantages of the coupled oscillators is their low phase noise performance compared to a single oscillator. Power is increased M times due to the presence of M oscillators but there are also M more noise sources. However, noise increases by $\sqrt{M}$ which results in an overall improvement in the phase noise performance by $\sqrt{M}$ times or $10\log(M)$ dB. The mechanical analogy in [15] provides an intuitive insight of the mechanism of noise reduction. Several coupled systems have more mass and hence more inertia than a single one and hence are more resistant to impulse displacements than a single system. However, some might argue that the phase noise improvement in M coupled oscillators should be different than the case where the power is increased by M times in a single oscillator because the coupling factor is much less than unity. An intuitive explanation can be made as follows: A single oscillator dissipating M times the power is equivalent to M in-phase oscillators connected in parallel. In both systems, any noise perturbation affects the whole system of oscillators and thus gets rejected by their large collective power (mass/inertia in the mechanical model) and hence, the phase noise is improved. On the other hand, for a weakly coupled system, the oscillators inject small currents into each other and hence require more time to correct for any perturbation that happens. Thus, noise perturbations will affect the coupled system differently according to the frequency of the noise.[1] Low frequency noise perturbations will allow the weakly coupled system enough time to respond and correct for this perturbation and hence achieve the phase noise improvement while fast perturbations or high frequency noise will experience less rejection from the coupled system. Hence, as will be seen from the results of the following analysis, the value of the coupling factor mainly affects the bandwidth of the phase noise improvement and not its value, i.e., the larger the coupling factor, the wider the bandwidth of phase noise improvement and vice versa.

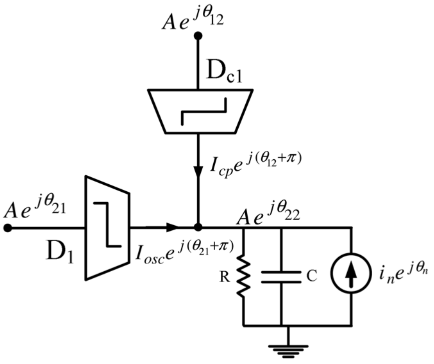

Fig. 7. Circuit model of node (2, 2) including the noise source.

The circuit model shown in Fig. 7 is similar to that in Fig. 5 except for additional noise currents modeling the total noise of the active devices of the main delays cells as well as the coupling cells. The noise current can be viewed as an injection-locking signal which pulls the oscillator frequency and hence, changes

---

[1] In an oscillating system, this noise frequency is measured as an offset from the oscillation frequency.

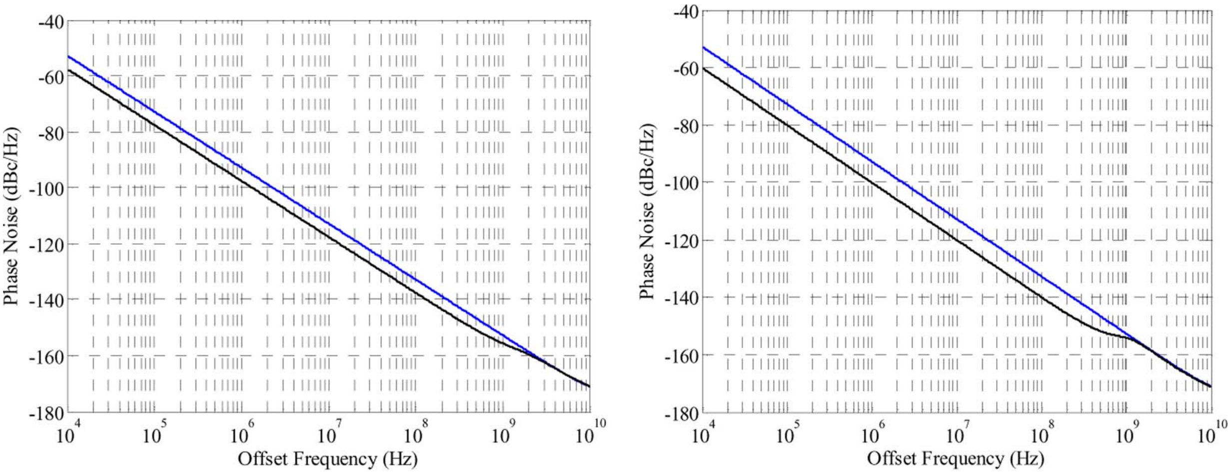

(a) (b)

Fig. 8. Calculated phase noise plot for the case of (a) $N = M = 3$ CCRO and (b) $N = 3$, $M = 5$ CCRO, with $k = 0.1$.

its phase [12]. We model the noise in a 1 Hz bandwidth at a frequency ω_m offset from the oscillation frequency ω_0 as $i_n e^{j\theta_n}$ where $\theta_n = (\omega_0 + \omega_m)t$. Accordingly, we can apply the previous analysis but including this noise current. The phase equation given in (2) is modified to be

$$\frac{d\theta_{22}}{dt} = \frac{1}{RC} \times \frac{I_{osc}\sin(\theta_{21}-\theta_{22})+I_{inj}\sin(\theta_{12}-\theta_{22})-i_n\sin(\theta_n-\theta_{22})}{I_{osc}\cos(\theta_{21}-\theta_{22})+I_{inj}\cos(\theta_{12}-\theta_{22})-i_n\cos(\theta_n-\theta_{22})}. \tag{13}$$

Applying the perturbation analysis and simplifying we can arrive at the phase noise expression at a frequency offset ω_m as detailed in Appendix B and given here for convenience.

$$\begin{aligned}\mathcal{L}(\omega_m) &= \frac{S_\theta(\omega_m)}{2} \\ &= \frac{8kT}{R}\frac{(a^2+b^2)}{I_{osc}^2 b^4}\frac{1}{\left|\det(\underline{P^M}+\underline{C^M})\right|^2} \\ &\quad\times\Bigg[\left|\underline{P^{M-1}I}\right|^2+\left|\underline{P^{M-2}CI}\right|^2 \\ &\quad+\left|\underline{P^{M-3}C^2I}\right|^2+\cdots+\left|\underline{C^{M-1}I}\right|^2\Bigg]\end{aligned} \tag{14}$$

where $\underline{P}$, $\underline{C}$, a and b are functions of k, ψ_0, ϕ_0, ω_m, R and C as defined in Appendix B.

The phase noise of a single-loop ring oscillator can be obtained by substituting $k = 0$ in the analysis above and is given by

$$\mathcal{L}(\omega_m) = \frac{2S_n(\omega_m)}{I_{osc}^2}\frac{1}{\left|\left(1+jRC\omega_m\cos^2\left(\frac{\pi}{N}\right)\right)^N-1\right|^2} \times\frac{\left|1+jRC\omega_m\cos^2\left(\frac{\pi}{N}\right)\right|^{2N}-1}{\left|1+jRC\omega_m\cos^2\left(\frac{\pi}{N}\right)\right|^2-1}. \tag{15}$$

This expression can be proven to match the expression derived in [12]. For a fair comparison between the phase noise of the CCRO and a single ring oscillator, we should note the following:

1) The total current used in one stage of the CCRO should be equal to that of the single-loop oscillator case. From the analysis done before: $I_t = I_{osc}\sqrt{a^2+b^2}$.
2) For the case where $N \neq M$ in the CCRO, the oscillation frequency of the CCRO deviates from that of the single-loop ring oscillator as given in (11). This change in frequency should also be accounted for when calculating the final phase noise improvement because phase noise degrades at higher frequencies.

We now substitute with numerical values in (14) and (15), and compare the phase noise of the CCRO with that of a single-loop ring oscillator. A 3 GHz oscillator with a current of $I_{osc} = 7$ mA and $k = 0.1$ is assumed for the calculations and only thermal noise is considered. Fig. 8 plots the phase noise for the cases of $N = 3$, $M = 3$ and $N = 3$, $M = 5$. As can be observed from the figure, the phase noise of the CCRO is less than that of a single ring oscillator by $10\log(M)$ over the lower range of frequency offsets (the phase noise improvement bandwidth) and then degrades and follows that of the single ring oscillator for higher frequencies offsets. Fig. 9 shows the phase noise improvement bandwidth for coupling factors $k = 0.01$, 0.1 and 0.2, for the cases of $N = 3$, $M = 3$ and $N = 3$, $M = 5$. As mentioned before the coupling factor affects the bandwidth only and not the value of the phase noise improvement.

We also have to note that the transconductances of the coupling stages are k times smaller than the main delay cells and hence their output noise currents are k times smaller. Hence, for ranges of k from 0.2–0.01, shown in Fig. 9, the coupling stages' noise is 7 to 40 dB smaller. Therefore the noise of the main delays cells is mostly dominant. However increasing the coupling factor further makes the noise of the coupling stages comparable to the main delay cells'. Also the output impedance becomes comparable and hence the frequency of operation drops. Taking these two effects into consideration one can find the overall change in the phase noise of the coupled system.

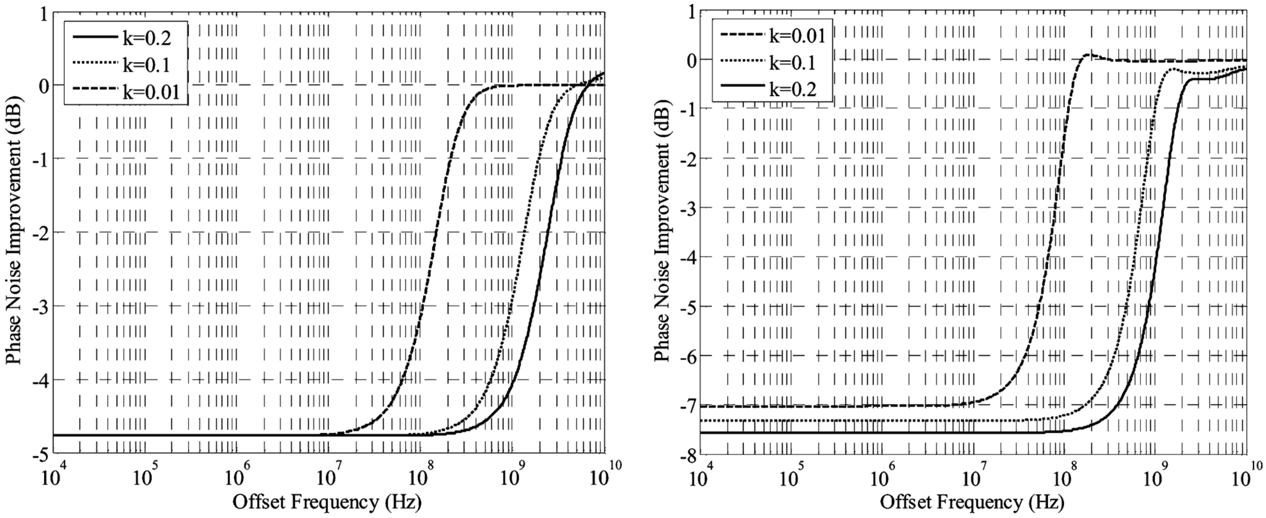

(a)

(b)

Fig. 9. Calculated phase noise improvement for the case of (a) $N = M = 3$ CCRO and (b) $N = 3$, $M = 5$ CCRO, for $k = 0.01$, 0.1 and 0.2.

TABLE I
PHASE SHIFTS REQUIRED FOR DIFFERENT N-PUSH OPERATIONS

Number of Signals	Phase shifts	Preserved Harmonics	Cancelled Harmonics	Output type
2	0°,180°	2, 4, 6, …	1, 3, 5, …	Single
2	0°, 90°, 180°, 270°	2, 4, 6, …	1, 3, 5, …	Differential
2	(0°, 90°, 180°, 270°), (45°, 135°, 225°, 315°)	2, 4, 6, …	1, 3, 5, …	I,Q
3	0°,120°, 240°	3, 6, 9, …	1, 2, 4, 5, …	Single
3	0°, 60°, 120°, 180° 240°, 300°	3, 6, 9, …	1, 2, 4, 5, …	Differential
4	0°, 90°, 180°, 270°	4, 8, 12, …	1, 2, 3, 5, 6, 7, …	Single
5	0°, 72°, 144°, 216°, 288°	5, 10, 15, …	1, 2, 3, 4, …	Single

III. N-PUSH CCRO

A. N-Push Technique

N-push techniques have been used in literature to generate a higher frequency signal from a lower frequency oscillator [10], [16]–[18]. The simplest example used for illustration is that adding two out-of-phase signals cancels the fundamental tone as well as the odd harmonics and preserves the even ones. This can be extended to N-signals with $2\pi/N$ phase differences to produce the Nth harmonic while cancelling all lower order ones. Table I shows examples detailing the number of needed signals and their phase shifts that when added together cancels some harmonics and enforces others. It also details the number of phases needed for single, differential and I-Q outputs for the case of frequency doubling. Consequently to apply the N-push techniques to the output of an oscillator, it needs to have a multi-phase output providing the required phases as well as a limiting circuit that ensures that these signals are rich in harmonics. The order of the phase shifted signals is not important in the N-push operation as long as all phase shifts are available. The price of having a higher frequency is an increase in the power and area of the N-push oscillator. Also, phase noise degrades by a factor of N^2 or $20\log(N)$ dB due to frequency multiplication.

Ring oscillators inherently provide different phase shifted signals, and so the N-push technique can be used with significantly less area and power overhead than the LC counterparts. In this work we propose to use the N-Push technique with CCROs to obtain a low phase noise wideband oscillator as well as a low phase noise mm-wave oscillator. We illustrate that for the proposed N-Push CCRO, a higher FOM can be obtained as described in the two design cases presented next.

B. Design Cases of N-Push CCRO

1) A Wideband 3–12.8 GHz N-Push/M-Push CCRO: The first design demonstrates a wideband oscillator with a very wide tuning range using an oscillator with a smaller tuning range [11]. As mentioned before, the proposed CCRO provides N signals phase shifted by $\phi_0 = \pi + \pi/N$ and provide M sets of those N-signals shifted by $\psi_0 = \pi + (2n+1)\pi/M$ (where $n \in \mathbb{Z}$ and $0 < n < M/2$). Hence, we can apply the N-Push technique to the N signals and M-Push to the M signals to provide two output signals. By suitable choice of the ring oscillator's operating frequency, N, and M, a wide tuning range can be achieved.

In this work, five three-stage ring oscillators $(N=3,\ M=5)$ operating at 1–2.5 GHz using CMOS inverters as delay cells

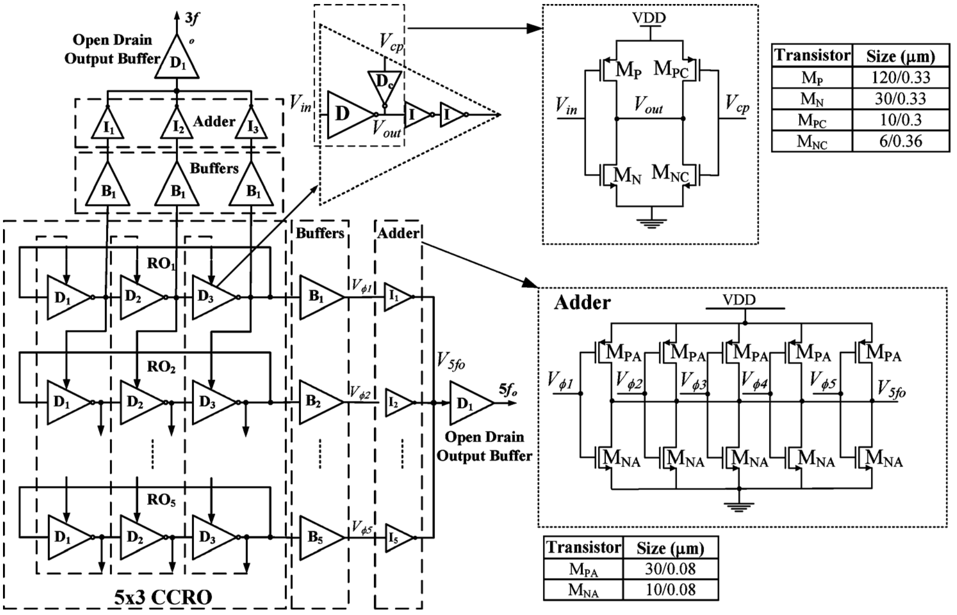

Transistor	Size (μm)
M_P	120/0.33
M_N	30/0.33
M_{PC}	10/0.3
M_{NC}	6/0.36

Transistor	Size (μm)
M_{PA}	30/0.08
M_{NA}	10/0.08

Fig. 10. Circuit diagram of the wideband N-Push/M-Push CCRO.

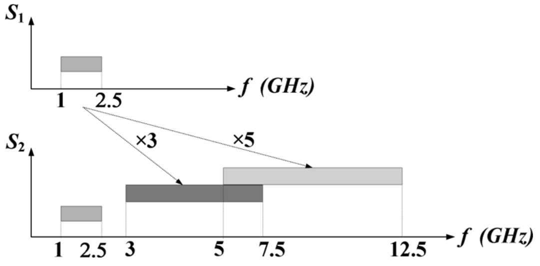

Fig. 11. The output frequency spectrum of the wideband CCRO showing the bandwidth extension due to the combined N-push/M-push operation.

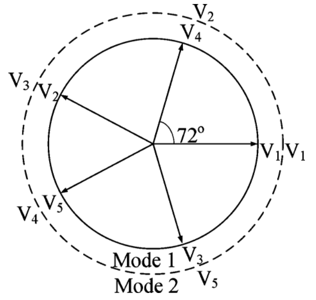

Fig. 12. The phasor diagram of the relative voltage phases of the different ring oscillators within the CCRO showing the two stable modes for $M = 5$.

are coupled to form the CCRO shown in Fig. 10. The three vertical outputs are added together using an adder stage made of three CMOS inverters with the outputs tied together to generate the third harmonic tone and cancel the fundamental tone. The five horizontal signals are added in a similar fashion to produce the fifth harmonic as shown in Fig. 10. The N-Push/M-Push CCRO is tuned by changing the supply voltage of the delay cells. Ring oscillators can also be tuned by the use of varactors, similar to the case of LC oscillators, without changing the supply voltage. Hence, eliminating any power variation associated with changing the supply voltage. However, using varactors will provide a much smaller frequency gain, K_{VCO}, and hence less frequency tuning range. In addition, if varactors were to be used they should be placed at all output nodes of the ring oscillator to preserve the phase shift balance between the output nodes which consumes more area.

Illustration of the proposed frequency planning is depicted in Fig. 11. The N-Push output range is 3–7.5 GHz (frequency multiplication by 3) while the M-Push range is 5–12.5 GHz (frequency multiplication by 5) giving an overall continuous range of 3–12.5 GHz. This output has a tuning range (defined as the bandwidth divided by the center frequency) of 122.6%. Moreover, including the 1–2.5 GHz range increases the tuning range to 163%. Potential applications of such oscillator would be software defined radios supporting several standards and the IEEE 802.16a (2–11 GHz) standard. This N-Push/M-Push CCRO can also be used with UWB if employed within a digital PLL with fast settling times satisfying the stringent requirements of UWB.

This great boost in frequency tuning range can relax the design of oscillators and dividers required for wideband applications. Oscillators can have a lower K_{VCO} and hence lower noise and dividers can have lower operation frequency, tuning range and hence power consumption. In addition, this topology enables the core ring oscillator of the CCRO to run at a lower frequency. Hence, we can use larger devices for the delay cells (120 μm/330 nm for the PMOS and 30 μm/330 nm for the NMOS) which lowers the phase noise as well as reduces the mismatches between transistors. Moreover the CCRO has a lower phase noise than a single ring oscillator by M times.

We should recall here that several modes given by (8) can be stable within the CCRO as proved before. We notice that these modes have the same set of equally spaced phase-shifted signals but in different order, as illustrated in Fig. 12 for the case of $M = 5$. Hence, for any stable mode the M-Push CCRO will still work properly. This is because the M-Push technique only

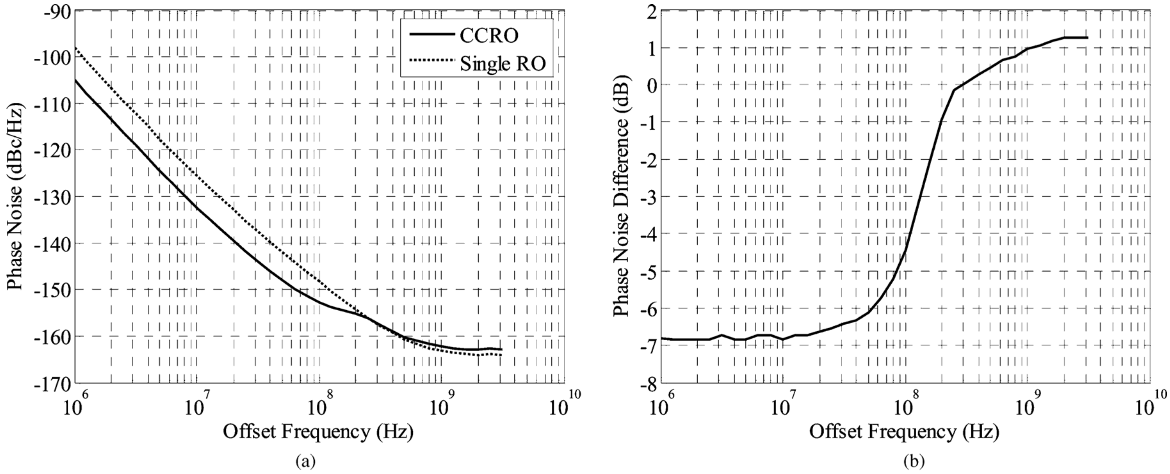

(a) (b)

Fig. 13. (a) Simulated phase noise plots and (b) phase noise difference of the reference N-push oscillator versus the N-Push/M-Push CCRO.

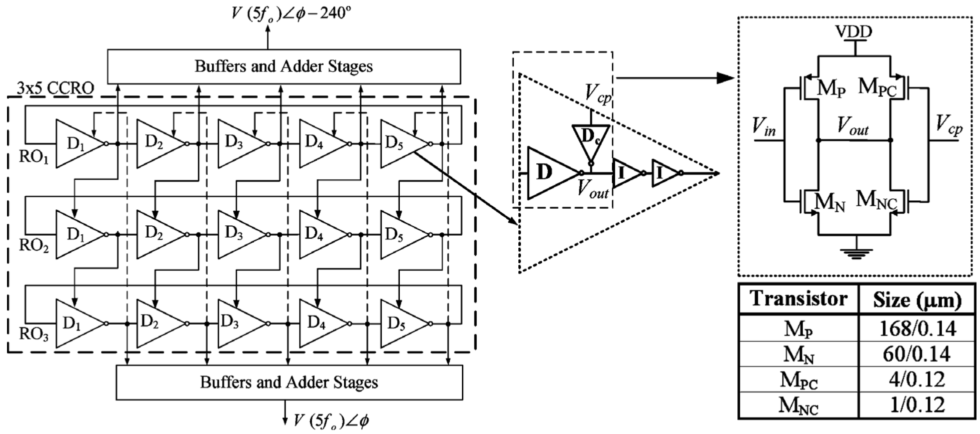

Transistor	Size (μm)
M_P	168/0.14
M_N	60/0.14
M_{PC}	4/0.12
M_{NC}	1/0.12

Fig. 14. Circuit diagram of the mm-wave N-push CCRO showing the two outputs having different phases.

needs M equally spaced phase-shifted signals (in any order) to work correctly. There will be a slight shift in the frequency of different modes (depending on ψ_0 as given by (12)) which can be easily compensated by the PLL loop.

A reference N-push oscillator with a single-loop three stage ring oscillator $(M = 1,\ N = 3)$ is also designed and included for comparison of the phase noise. The core ring oscillator uses inverters with transistors having the same sizes as the proposed CCRO. Fig. 13(a) shows the phase noise simulation plots of the reference N-push oscillator versus the N-Push/M-Push CCRO. An improvement in the phase noise of 6.9 dB is observed for a bandwidth of nearly 100 MHz and then both curves coincide as shown in Fig. 13(b).

2) Millimeter-Wave 13–25 GHz N-Push CCRO: The second design illustrates the advantage of the CCRO in providing a low phase noise multi-phase millimeter-wave (mm-wave) frequency output. Recall that M coupled ring oscillators have M times less phase noise than a single-loop ring oscillator. Also, increasing the power consumption by M times in ring oscillators reduces the phase noise by M times due to faster transitions for the output signal. Hence, some might argue that to achieve a phase noise performance similar to that of the CCRO we can just spend the same amount of power in a single ring oscillator. This might be true for lower frequencies; however, it has practical limitations at mm-wave frequencies. High currents flowing in the transistors and interconnects necessitates that metal lines have enough width to accommodate those high currents without inducing reliability issues such as electro-migration problems. Doing so adds more parasitic capacitances to the transistors' output node which limits the highest achievable frequency of operation. In particular at mm-wave frequencies, transistors are sensitive to any slight addition of capacitance. In [19], the upper bound of the achievable phase noise in a ring oscillator was derived and proven to be dependent on the f_T of the process. However, here we use the coupled structure to reduce the phase noise beyond what is achievable from a single ring oscillator.

In addition, the N-push operation allows the ring oscillator to run at a lower frequency. This permits the use of non minimum dimensions in the delays cells of the ring oscillator. Since flicker noise current is inversely proportional to the transistor length and width as given by [20]

$$\frac{\overline{i_n^2}}{\Delta f} = \frac{K}{f}\frac{g_m^2}{WLC_{ox}^2}, \tag{16}$$

increasing W and L while maintaining a constant g_m reduces flicker noise significantly [21]. Also, by sizing the PMOS to be 3–4 times the NMOS, symmetry is ensured in the output signal

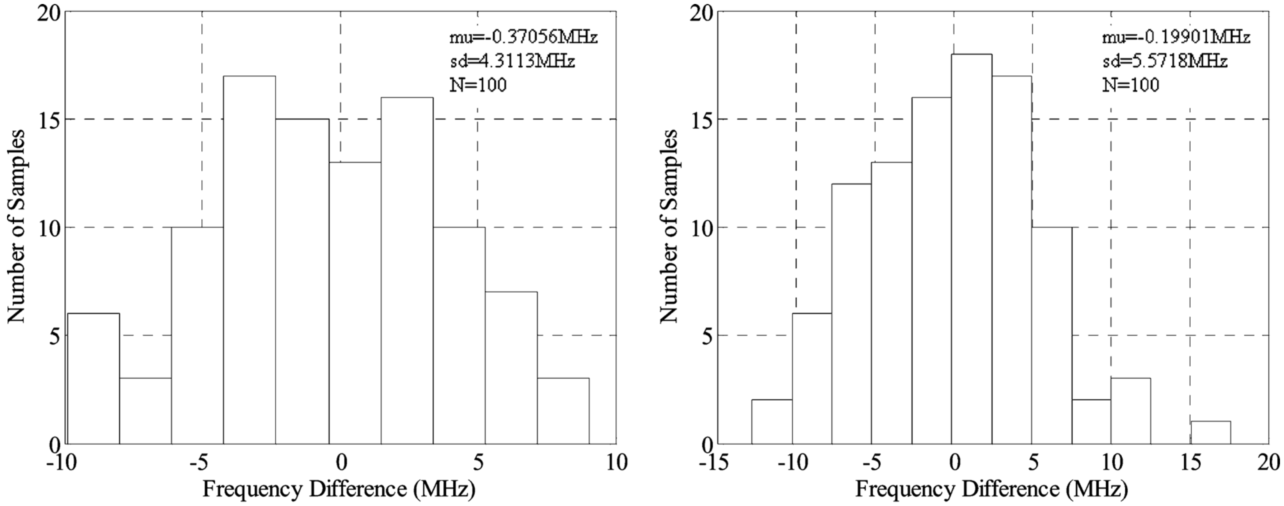

(a) (b)

Fig. 15. Monte Carlo simulation showing the distribution of the difference in oscillation frequency between two free running oscillators within the proposed CCROs at (a) 2.6 GHz (b) 4.5 GHz.

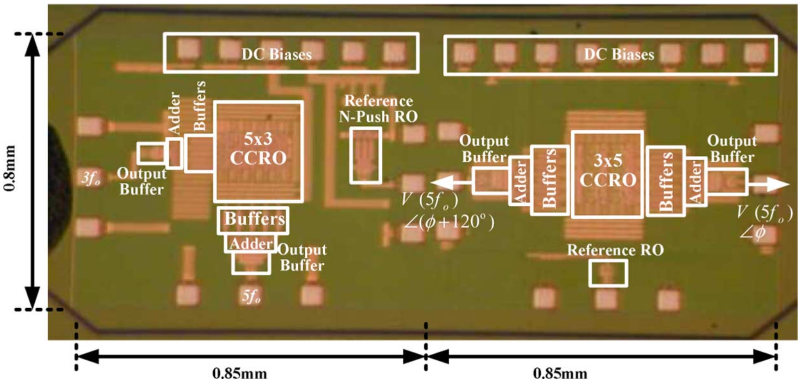

Fig. 16. Chip micrograph.

which leads to a 50% duty cycle signal which means absence of lower order even harmonics, providing a clean spectrum.

The final advantage of the N-Push CCRO is the availability of different phases of this mm-wave frequency signal. Applying N-push to the outputs of each ring oscillator within the CCRO can provide M multi-phase signals. These mm-wave multi-phase signals can be used in mm-wave image reject receivers [1], high speed samplers or time interleaved applications [2] increasing their frequencies of operation.

A three five-stage CCRO $(N = 5,\ M = 3)$ is presented in Fig. 14. The five output signals have a progressive phase delay of $\phi = 216^\circ$ in the horizontal direction. In the vertical direction the phase delay between successive oscillators is $\psi = 240^\circ$. The core ring oscillator produces an output frequency range of 2.6–5 GHz and uses non-minimum lengths of 140 nm to reduce flicker noise. The coupling factor between the ring oscillators is 0.022 to reduce any capacitive loading from the coupling stages. The coupling factor can be approximated as the ratio of the aspect ratios (shown in Fig. 14) of the main delay cell to that of the coupling delay cell. The outputs of five stage oscillator are buffered and added (using the same adder shown in Fig. 10) to produce an output of 13–25 GHz. Similarly, the outputs signals of a second oscillator are combined to produce the same 13–25 GHz signal but with a -240° phase shift as illustrated in Fig. 14. Hence, we provide a proof of concept that applying N-Push operation to the two sides of a CCRO can produce mm-wave multi-phase outputs.

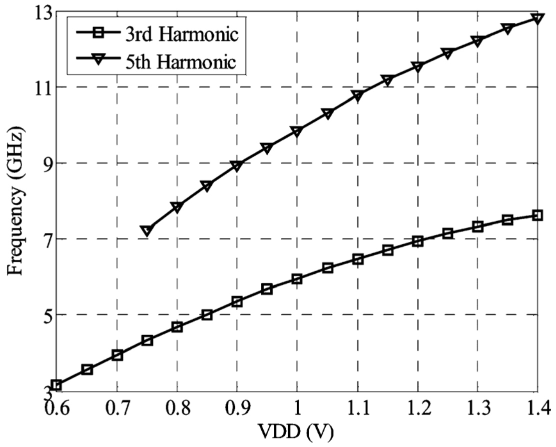

Fig. 17. Measured frequency tuning curve of the wideband 5×3 N-push/M-push CCRO.

A general note on the abovementioned CCROs is that mismatches between the oscillators within the CCRO can result in each oscillator having a slightly different oscillation frequency. To ensure proper operation of the CCRO this frequency shift should be always kept within the locking range of the oscillators (which actually depends on the coupling factor). Hence, the

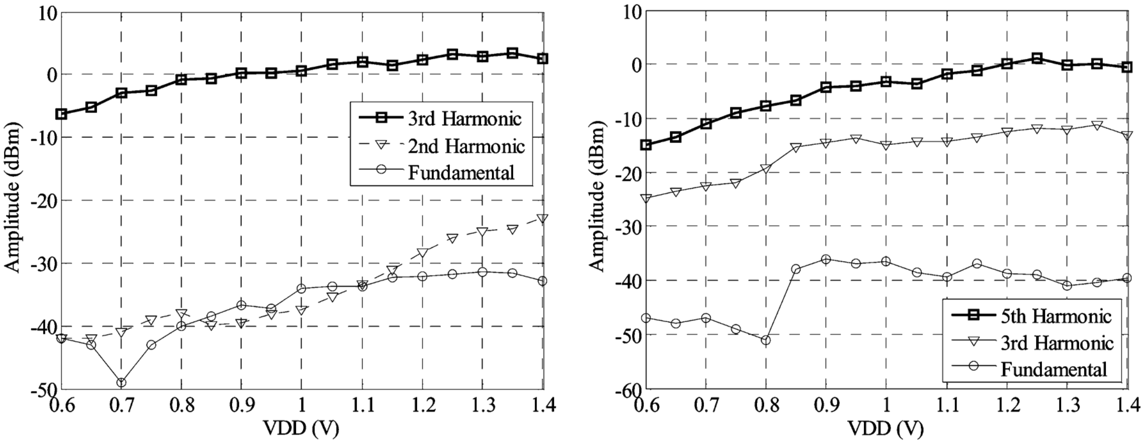

(a) (b)

Fig. 18. Measured amplitudes of the fundamental and harmonics tones for (a) the N-Push ($N = 3$) and (b) M-Push ($M = 5$) outputs.

minimum acceptable coupling factor should ensure a locking range wider than the shift in the oscillation frequency due to mismatches between the oscillators within the CCRO.

We run Monte Carlo simulations and calculate the shift in oscillation frequencies between the oscillators within the designed CCROs (when uncoupled). As shown in Fig. 15, the 3σ of the oscillation frequency difference is limited to 15 MHz for both our designs. The locking range is actually equivalent to the bandwidth over which the phase noise improves and hence can be calculated from Fig. 9. For example, for a coupling factor of 0.01, the locking range is 70–100 MHz which is much higher than the standard deviation of the oscillation frequency difference.

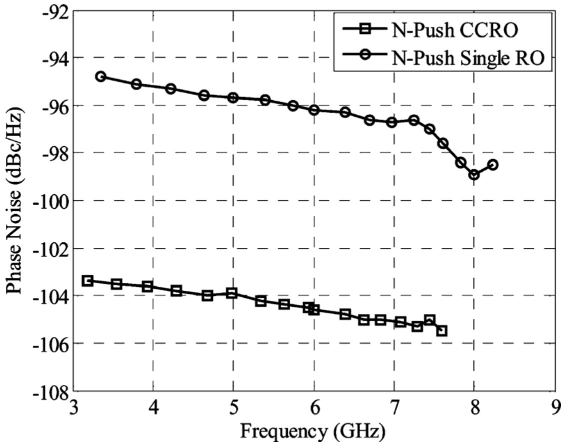

Fig. 19. Measured phase noise improvement at 1 MHz offset of the CCRO.

IV. MEASUREMENT RESULTS

The proposed cyclic coupled ring oscillators are implemented in a 90 nm digital regular V_T CMOS process with nine metal layers. The chip micrograph, shown in Fig. 16, depicts the two designs: the wideband 3–12.5 GHz 5×3 N-Push/M-Push CCRO and the mm-wave 13–25 GHz 3×5 N-push CCRO. They occupy an active area of 0.145 mm^2 and 0.135 mm^2, respectively. The outputs were tested using on-wafer probing, and the spectrum was measured using the Agilent E4446, 44 GHz, power spectrum analyzer. However, since both ring oscillators are free running, measuring the phase noise using the E4446 is not accurate due to drifting of the oscillator tone. Thus, we used the Agilent E5052B 10 MHz–7 GHz signal source analyzer combined with the Agilent E5053A 3 GHz–26.5 GHz microwave down-converter to be able to accurately measure the phase noise. Agilent E5052B uses a wideband frequency discriminator technique which can capture the phase noise of drifting signals.

A. Wideband 3–12.8 GHz N-Push/M-Push CCRO

We first present the measurement results of the wideband 3–12.8 GHz N-Push/M-Push CCRO with $N = 3$, $M = 5$. Fig. 17 shows the frequency of the N-Push output of this oscillator at $3f_o$ as well as the M-Push output at $5f_o$ versus the tuning voltage. The oscillators are tuned by changing their supply voltage. This figure illustrates the continuous frequency operation from 3.16–12.8 GHz with a frequency overlap from 7.24–7.6 GHz. Fig. 18(a) and (b) present the output harmonics for the N-Push and M-push outputs respectively. They also show the cancelled lower order harmonics. The fundamental tone has more than 30 dB of rejection for the N-Push and 40 dB for the M-Push. Although simulations predict 45 dB of suppression for the third harmonic (similar to the fundamental tone), it is observed to have only 11 dB of rejection in the M-push case. This is attributed to supply coupling from the N-Push output to the M-push output, as buffers and adders of both stages share the same supply lines. A more optimized design could turn off the output not in use to avoid this effect.

The reference N-push oscillator is also designed and fabricated for comparison. It runs from 1.11–2.74 GHz with the N-push output at 3.35–8.23 GHz, which is close to the frequency of the proposed CCRO. The phase noise curves of both oscillators are plotted in Fig. 19. A difference of around 8 dB is observed over the frequency range which is close to the theoretical value of 7.57 dB for a coupling factor of 0.2 as shown before in Fig. 8. This confirms the $10\log(M)$ phase noise improvement for the proposed coupled topology experimentally. Fig. 20(a) and (b) illustrate the amplitude and phase noise of both the N-push and M-push outputs of the wideband

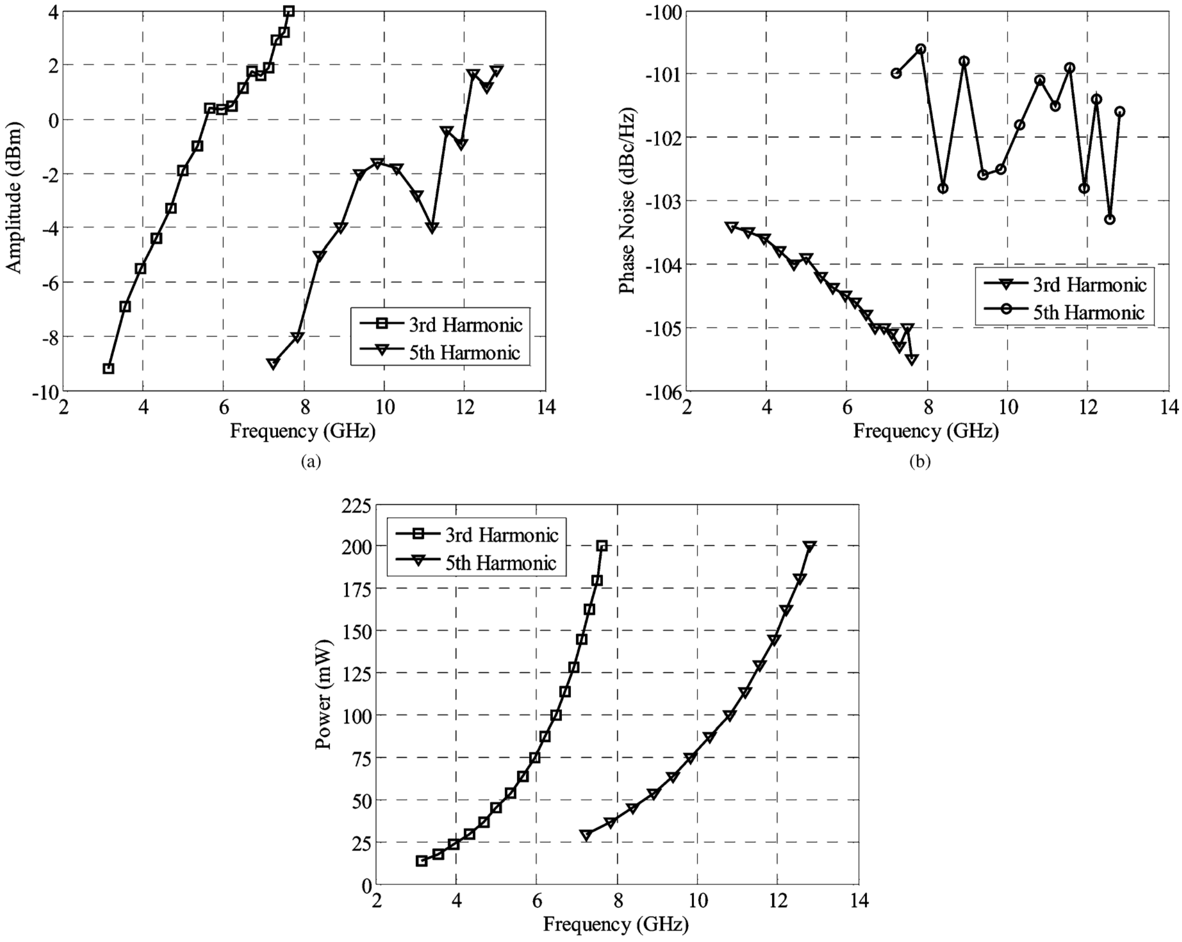

(a) (b) (c)

Fig. 20. (a) Measured amplitude and (b) phase noise of the output as well as (c) the power consumption of the wideband 5 ×3 N-push/M-push CCRO.

TABLE II
COMPARISON OF THE PERFORMANCE OF THE WIDEBAND 5 ×3 N-PUSH/M-PUSH CCRO WITH PREVIOUSLY PUBLISHED WORK

	Frequency Range (GHz)	**Tuning Range (%)**	**Phase noise @ 1MHz (dBc/Hz)**	**Power consumption (mW)**	**Technology (CMOS)**	***FOM$_T$***
This Work	1 – 2.56 3.16 – 12.8	163	-105.5 @ 7.7GHz	13-200	90nm	-184.4 – -190.4
[23]	1.82 – 10.18	139.4	-88.4 @ 5.65 GHz	5	130nm	-179.34
[24]	2.5 – 9	113	-85 @ 5 GHz	135	180nm	-158.7
[25]	3 – 11	114	-88 @ 5 GHz	85	190nm	-163.8
[26]	1 – 9.4	161.5	-112.3 @ 10MHz @ 6GHz	7.4	130nm	-183.33
[27]	0.8 – 10	170.37	-90 @ 6.4GHz	6	120nm	-162.97
[28]	3 – 10	107.7	-	0.3-1	90nm	-
[29]	1 – 10.3	164.6	-	3.5-17.25	130nm	-

oscillator versus the output frequency. We observe nearly 2 dB degradation in phase noise due to the shift from frequency multiplication by 3 to multiplication by 5. Power consumption is conserved by switching between the two outputs, as the supply voltage can then be lowered, as shown in Fig. 20(c). The rms jitter (integrated from 100 KHz to 10 MHz) at the lowest (3.16 GHz) and highest (12.8 GHz) frequencies is measured to be 2.13 psec and 0.76 psec, respectively. To the best of the authors' knowledge, the performance of the proposed wideband N-Push/M-Push CCRO is one of the best reported in literature as shown in Table II. The proposed oscillator has the highest Figure of Merit for Tuning (FOM_T) defined as [22]

$$FOM_T = \mathcal{L}(\Delta f) - 20\log\left(\frac{f_0}{\Delta f}\frac{TR}{10}\right) + 10\log\left(\frac{P_{dc}}{1\mathrm{mW}}\right) \tag{17}$$

where $\mathcal{L}(\Delta f)$ is the phase noise at an offset frequency Δf, TR is the tuning range percentage and P_{dc} is the power consumption in mW.

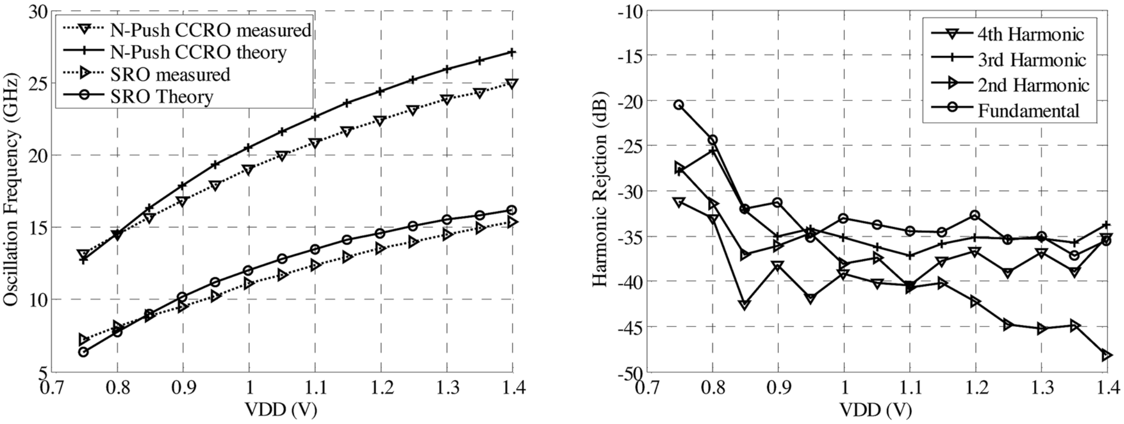

(a) (b)

Fig. 21. (a) Theoretical versus measured frequency tuning curves of the mm-wave 3×5 N-Push CCRO and the reference oscillator. (b) The amplitudes of the lower order harmonics for the mm-wave 3×5 N-Push CCRO.

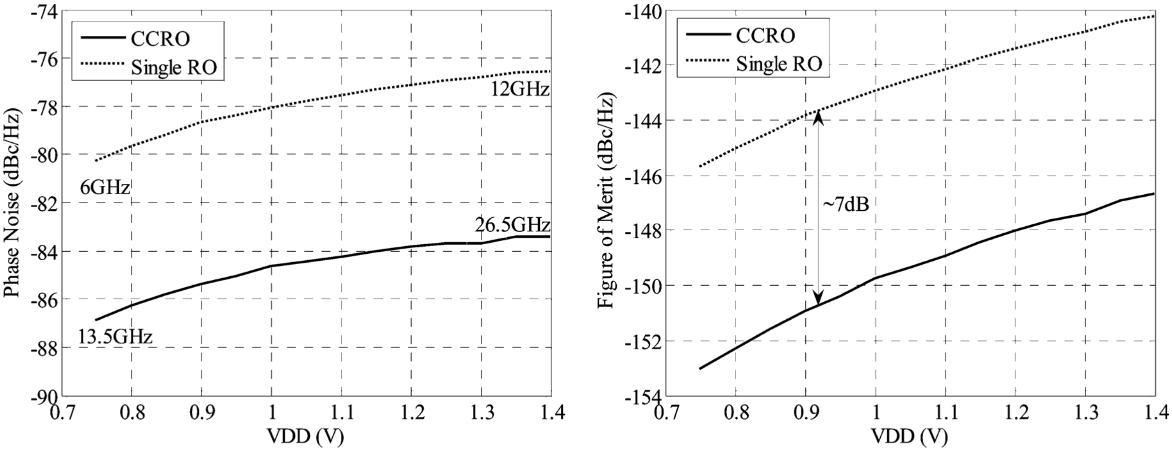

(a) (b)

Fig. 22. (a) Simulated phase noise at 1 MHz offset and (b) *FOM* comparison of the mm-wave *N*-Push CCRO and the reference single loop oscillator.

B. Millimeter-Wave 13–25 GHz N-Push CCRO

Second, we present the measurement results of the proposed millimeter wave 13–25 GHz 3×5 N-push CCRO. We also designed and fabricated a reference oscillator to compare with. This reference oscillator represents the fastest three-stage single loop inverter-based ring oscillator that the process allows. The loading to the oscillator is minimized through a six stage tapered buffer to drive the output buffer. Fig. 21(a) shows the measured frequency tuning curve of both oscillators. The reference oscillator has an output frequency range of 7.25–15.35 GHz, while the proposed oscillator has a higher frequency range of 13–25 GHz. To validate the analysis presented in Section II-B, the measured oscillation frequencies of both oscillators are plotted in Fig. 21(a) versus the theoretical values calculated from (5). The figure shows the same trend of frequency variation with the supply voltage. The difference in the frequency value is attributed to the fact that the resistance and the capacitance in (5) are estimated from a DC analysis while their values are voltage dependent and hence change throughout the oscillation cycle. The rejection of all the lower order harmonics is more than 35 dB over most of the tuning range as shown in Fig. 21(b). The simulated phase noise performance of the proposed CCRO as well as the reference one is shown in Fig. 22(a). Phase noise of the proposed oscillator is less than that of the reference oscillator by 6–7 dB over the tuning range. Since, the output frequencies and power consumptions are different it is more accurate to compare the Figure of Merit (FOM) of oscillators defined as

$$FOM = \mathcal{L}(\Delta f) - 20\log\left(\frac{f_0}{\Delta f}\right) + 10\log\left(\frac{P_{dc}}{1\mathrm{mW}}\right). \quad (18)$$

Fig. 22(b) shows that there is an improvement of 7 dB in the FOM of the proposed oscillator across the tuning range. On the other hand, Fig. 23(a) and (b) show the measured phase noise and FOM of both oscillators respectively. Measurement results show an improvement of 10–20 dB in the phase noise and 8.7–20.4 dB in the FOM of the proposed oscillator across the tuning range. The discrepancy in results may be attributed to several factors. First, measuring phase noise of free running oscillators is difficult even using the Agilent E5052 signal analyzer as the device cannot track the carrier tone accurately for signals with large frequency drifts (due to high flicker noise). This is more pronounced in the reference oscillator due to its

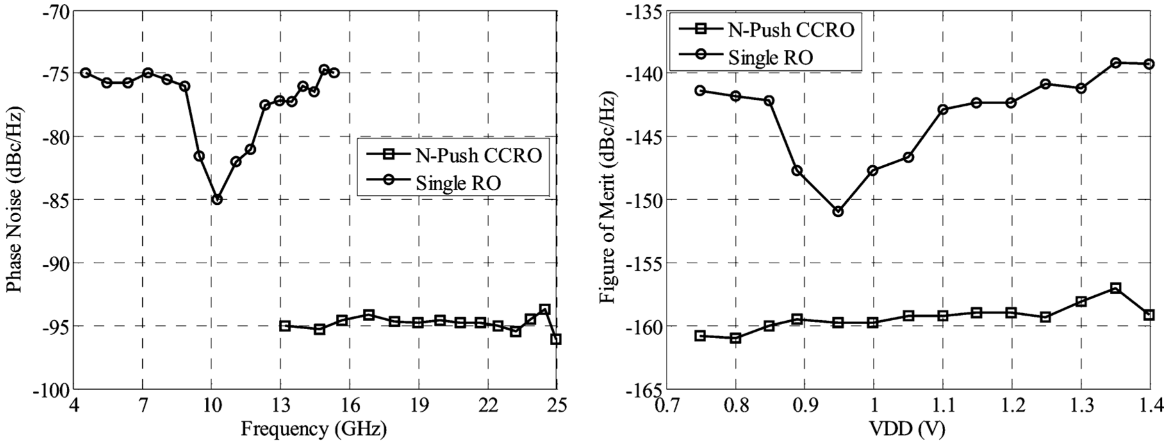

(a) (b)

Fig. 23. (a) Measured phase noise at 1 MHz offset and (b) FOM comparison of the mm-wave N-Push CCRO and the reference single loop oscillator.

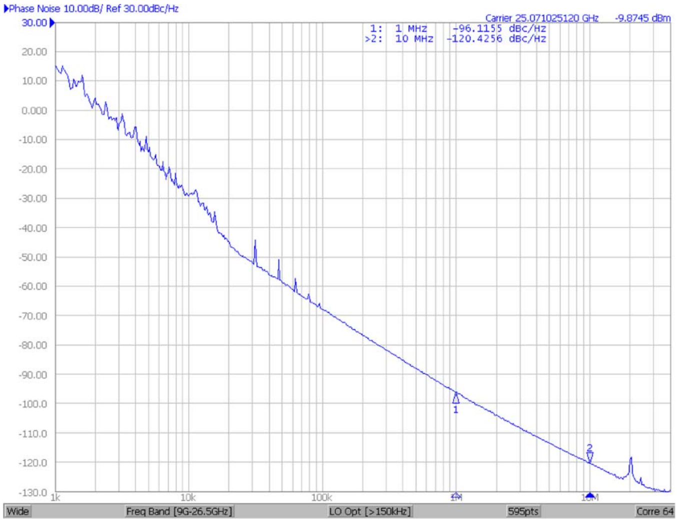

Fig. 24. Measured phase noise snapshot of the output of the mm-wave 3 × 5 N-Push CCRO at 25 GHz.

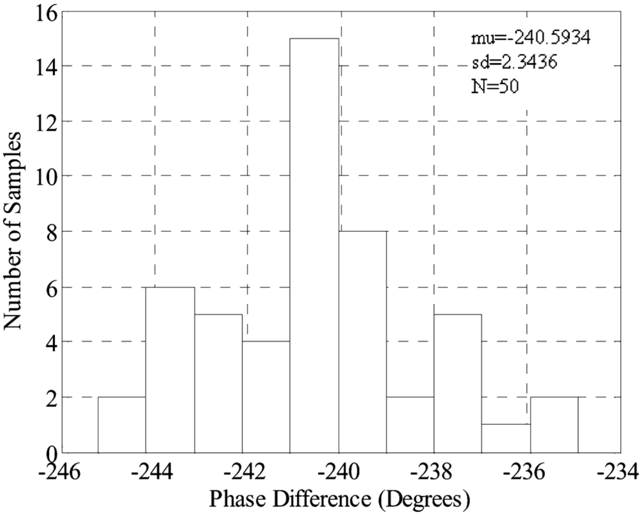

Fig. 25. Monte Carlo simulations showing the phase difference between the two outputs of the mm-wave 3 ×5 N-Push CCRO in presence of mismatches.

higher phase noise and could introduce measurement errors. However, measurements for the CCRO were more stable. Second, we suspect overestimation of flicker noise in the noise models. Lastly, the change in slope in the reference oscillator phase noise curve can be attributed to measurement errors due to switching between modes in the signal analyzer after 10 GHz. Fig. 24 depicts a snapshot of the phase noise of the proposed oscillator at the highest output frequency of 25 GHz achieving a phase noise of -120.4 dBc/Hz at a 10 MHz offset frequency. Measuring the phase difference of -240° or (120°) between the two high frequency N-push outputs was not possible in the lab due to its sensitivity to any path mismatches between the two outputs. However, the concept has been proved in the previously proposed oscillator where the M-Push output produced the expected output. Moreover we run Monte Carlo simulations to show that despite the possible mismatches between transistors the phase difference is still close to -240° or (120°). Fig. 25 illustrates the Monte Carlo simulation results showing a mean of -240.59° with a standard deviation of 2.34°. The proposed architecture could also be used to generate quadrature signals by using four differential delay stages in the ring oscillators $(N = 4)$ and determining M based upon the frequency multiplication factor desired. Finally, Table III shows a comparison with state of the art inductor-less ring oscillators at mm-wave frequencies. Our proposed mm-wave N-push oscillator provides competitive performance as well as the state-of-the-art FOM. Although, [34] uses a ring oscillator as well to carry out the triple push operation, however, the advantage of our design is the reduced phase noise due to the use of the CCRO and a CMOS structure with a symmetric waveform as well as the availability of several phases for the output at the high frequency.

V. CONCLUSION

In this work, N-push cyclic coupled ring oscillators are used to implement a low phase noise wideband oscillator as well as a low phase noise mm-wave oscillator. Wide tuning range is achieved because of the availability of multiple sets of phase shifts from the CCRO. Low phase noise is possible because the core ring oscillator runs at lower frequencies and hence can have

TABLE III
COMPARISON OF THE PERFORMANCE OF THE MM-WAVE 13–25 GHZ N-PUSH CCRO WITH PREVIOUSLY PUBLISHED WORK

	Freq Range (GHz)	**Tuning Range (%)**	**Phase noise @ 1MHz (dBc/Hz)**	**Power (mW)**	**Area (mm^2)**	**Technology / f_T (GHz)**	**Available Output phases**	**FOM**
This Work	13-25	63.16	-96.11 @ 25GHz	37-257	0.1350	90nm/140	0, 120, 240 (simulated)	-159.2 to -161.8
[30]	28.36-31.96	11.94	-85.3 @ 31.96GHz	87	0.0108	SiGe - HBT/120	Differential	-156
[31]	22.5-25.5	10.53	-87 @ 25GHz	240	0.0225	SiGe/45	Differential	-151.89
[32]	18.33 – 21.19	14.47	-83.33 @ 21.2 GHz	152	0.0180	SiGe- HBT /120	I/Q	-148.03
[33]	13.75-21.5	43.97	-90 @ 18.69GHz	130	0.1972	InP – HBT /100	Differential	-154.29
[34]	0.1-65.8	199.4	-86@ 25GHz	1.2-26.4	0.0168	90nm CMOS / 110	Single ended	-160
	0.2-34	197.66	-69.2 @ 34GHz	2-70	0.0247	0.13µm CMOS / 98	Single ended	-141.4
[35]	18.5-25	29.89	-85 @ 24.3GHz	105.6	0.1472	0.12µm SiGe BiCMOS /200	I/Q	-152.7

non-minimum length dimensions which reduce the noise contribution. In addition, the use of this coupling topology improves the phase noise by $10\log(M)$. The CCRO is analyzed using the generalized form of Adler's equation for injection locking. We prove that phase noise improvement due to coupling happens within a certain bandwidth which depends on the coupling strength. Outside this bandwidth the phase noise follows that of a single ring oscillator. The proposed oscillators achieve low phase noise with higher FOM than state-of-the-art work.

APPENDIX A

Here, we perform the perturbation analysis [6] to determine the stability of the different oscillation modes derived in (8). Adding a small signal perturbation $\hat{\theta}_{ij}$ to each θ_{ij} we can write

$$\begin{aligned}\theta_{22} &= \omega_0 t + \hat{\theta}_{22}\\ \theta_{12} &= \omega_0 t + \hat{\theta}_{12} + \psi_0\\ \theta_{21} &= \omega_0 t + \hat{\theta}_{21} + \phi_0.\end{aligned} \tag{19}$$

Substituting (19) in (2) and linearizing the equations assuming small perturbations, yields

$$RC\frac{d\hat{\theta}_{22}}{dt} = X\hat{\theta}_{21} + kY\hat{\theta}_{12} - (X+kY)\hat{\theta}_{22} \tag{20}$$

where

$$\begin{aligned}X &= \frac{1+k\cos(\phi_0-\psi_0)}{[\cos(\phi_0)+k\cos(\psi_0)]^2}\\ Y &= \frac{k+\cos(\phi_0-\psi_0)}{[\cos(\phi_0)+k\cos(\psi_0)]^2}.\end{aligned} \tag{21}$$

Also,

$$RC\frac{d\hat{\theta}_{32}}{dt} = X\hat{\theta}_{31} + kY\hat{\theta}_{22} - (X+kY)\hat{\theta}_{32}. \tag{22}$$

Hence, the phase equation relating the difference in phase perturbations is given by subtracting (22) from (20):

$$RC\frac{d\Delta\hat{\theta}_{22}}{dt} = X\Delta\hat{\theta}_{21} + kY\Delta\hat{\theta}_{12} - (X+kY)\Delta\hat{\theta}_{22} \tag{23}$$

where $\Delta\hat{\theta}_{22} = \Delta\hat{\theta}_{22} - \Delta\hat{\theta}_{32}, \Delta\hat{\theta}_{21} = \Delta\hat{\theta}_{21} - \Delta\hat{\theta}_{31}$ and $\Delta\hat{\theta}_{12} = \Delta\hat{\theta}_{12} - \Delta\hat{\theta}_{22}$.

Writing it in a matrix form to represent all nodes in the CCRO we arrive at (24) and (25) shown at the bottom of the next page, where the primary and coupling matrices, $\underline{P}$ and $\underline{C}$, are given by

$$\underline{P} = \begin{bmatrix} X+kY & 0 & \cdots & 0 & -X\\ -X & X+kY & 0 & \cdots & 0\\ 0 & -X & \ddots & \ddots & \vdots\\ \vdots & \ddots & \ddots & \ddots & 0\\ 0 & \cdots & 0 & -X & X+kY \end{bmatrix}_{N\times N} \tag{26}$$

$$\underline{C} = \begin{bmatrix} -kY & 0 & \cdots & 0\\ 0 & -kY & \ddots & \vdots\\ \vdots & \ddots & \ddots & 0\\ 0 & \cdots & 0 & -kY \end{bmatrix}_{N\times N} \tag{27}$$

and $\underline{\mathbf{0}} = \text{zeros}(N, N)$.

APPENDIX B

Here, we perform the perturbation analysis to determine the phase noise expression of the CCRO. Simplifying (13) we get

$$\begin{aligned}RC\frac{d\hat{\theta}_{22}}{dt} = {}& X\hat{\theta}_{21} + kY\hat{\theta}_{12} - (X+kY)\hat{\theta}_{22}\\ &+ \frac{i_n\sqrt{a^2+b^2}}{I_{osc}b^2}\cos(\omega_m t + \gamma)\end{aligned} \tag{28}$$

where X and Y are the same as defined before and a, b and γ are defined as

$$\begin{aligned} a &= \sin(\phi_0) + k\sin(\psi_0) \\ b &= \cos(\phi_0) + k\cos(\psi_0) \\ \gamma &= \tan^{-1}\left(\frac{b}{a}\right). \end{aligned} \tag{29}$$

Assuming that this periodic noise perturbation results in a periodic change in the phases at ω_m, we can write (28) in a phasor form as

$$\begin{aligned} \left[(X + kY) + j\omega_m RC\right]\hat{\Theta}_{22} &= X\hat{\Theta}_{21} \\ &\quad + kY\hat{\Theta}_{12} + \frac{i_n\sqrt{a^2+b^2}}{I_{osc}b^2}e^{j\gamma} \end{aligned} \tag{30}$$

which in matrix form for all nodes of the CCRO becomes (31) and (32) shown at the bottom of this page, where $n_{22} = i_n \sqrt{a^2+b^2}/I_{osc}b^2 e^{j\gamma}$ which corresponds to the noise current injected at node (2, 2), i.e., second row and second column. The matrix $\underline{C}$ is the same as (27) but $\underline{P}$ changes to (33) shown at the bottom of the next page.

The inversion of $[A]$ can be proven to take this form:

$$\frac{d}{dt}[\Delta\hat{\theta}] = [A][\Delta\hat{\theta}] \tag{24}$$

$$\frac{d}{dt}\left[\begin{array}{c} \Delta\hat{\theta}_{11} \\ \vdots \\ \Delta\hat{\theta}_{1N} \\ \hdashline \Delta\hat{\theta}_{21} \\ \vdots \\ \Delta\hat{\theta}_{2N} \\ \hdashline \vdots \\ \hdashline \Delta\hat{\theta}_{M1} \\ \vdots \\ \Delta\hat{\theta}_{MN} \end{array}\right]_{MN\times 1} = \frac{-1}{RC}\left[\begin{array}{c:c:c:c:c} \underline{P} & \mathbf{0} & \cdots & \mathbf{0} & \underline{C} \\ \hdashline \underline{C} & \underline{P} & \mathbf{0} & \cdots & \mathbf{0} \\ \hdashline \mathbf{0} & \underline{C} & \ddots & \ddots & \vdots \\ \hdashline \vdots & \ddots & \ddots & \ddots & \mathbf{0} \\ \hdashline \mathbf{0} & \cdots & \mathbf{0} & \underline{C} & \underline{P} \end{array}\right]_{MN\times MN}\left[\begin{array}{c} \Delta\hat{\theta}_{11} \\ \vdots \\ \Delta\hat{\theta}_{1N} \\ \hdashline \Delta\hat{\theta}_{21} \\ \vdots \\ \Delta\hat{\theta}_{2N} \\ \hdashline \vdots \\ \hdashline \Delta\hat{\theta}_{M1} \\ \vdots \\ \Delta\hat{\theta}_{MN} \end{array}\right]_{MN\times 1} \tag{25}$$

$$[\hat{\Theta}] = [A]^{-1}[n] \tag{31}$$

$$\left[\begin{array}{c} \hat{\Theta}_{11} \\ \vdots \\ \hat{\Theta}_{1N} \\ \hdashline \hat{\Theta}_{21} \\ \vdots \\ \hat{\Theta}_{2N} \\ \hdashline \vdots \\ \hdashline \hat{\Theta}_{M1} \\ \vdots \\ \hat{\Theta}_{MN} \end{array}\right]_{MN\times 1} = \frac{-1}{RC}\left[\begin{array}{c:c:c:c:c} \underline{P} & \mathbf{0} & \cdots & \mathbf{0} & \underline{C} \\ \hdashline \underline{C} & \underline{P} & \mathbf{0} & \cdots & \mathbf{0} \\ \hdashline \mathbf{0} & \underline{C} & \ddots & \ddots & \vdots \\ \hdashline \vdots & \ddots & \ddots & \ddots & \mathbf{0} \\ \hdashline \mathbf{0} & \cdots & \mathbf{0} & \underline{C} & \underline{P} \end{array}\right]^{-1}\left[\begin{array}{c} 0 \\ \vdots \\ 0 \\ \hdashline 0 \\ n_{22} \\ \vdots \\ 0 \\ \hdashline \vdots \\ \hdashline 0 \\ \vdots \\ 0 \end{array}\right]_{MN\times 1} \tag{32}$$

$$[A]^{-1} = \frac{1}{\det(\underline{P^M} + \underline{C^M})} \times \begin{bmatrix} \underline{P^{M-1}} & \underline{C^{M-1}} & \cdots & \underline{P^{M-2}C} \\ \underline{P^{M-2}C} & \underline{P^{M-1}} & \cdots & \underline{P^{M-3}C^2} \\ \underline{P^{M-3}C^2} & \underline{P^{M-2}C} & \cdots & \underline{P^{M-4}C^3} \\ \vdots & \vdots & \cdots & \vdots \\ \underline{C^{M-1}} & \underline{PC^{M-2}} & \cdots & \underline{P^{M-1}} \end{bmatrix}_{MN\times MN} \tag{34}$$

It should be noted that successive rows and columns of the above matrix contain the same terms but shifted by one position. From (31) and (34), we observe that the noise n_{22} injected at node (2, 2) affects all other nodes in the coupled oscillator. Hence, to find the effect of the noise currents injected into all nodes of the coupled oscillator, the noise vector n is modified to

$$[n] = (i_n\sqrt{a^2+b^2}/I_{osc}b^2)e^{j\gamma}\begin{bmatrix}1 & 1 & \cdots & 1\end{bmatrix}^T_{MN\times 1}$$

and all phase variations are added as the mean square to yield

$$\begin{bmatrix}\bar{\hat{\Theta}}_i^2\end{bmatrix}_{N\times 1} = \frac{\bar{i}_n^2(a^2+b^2)}{I_{osc}^2 b^4}\frac{1}{|\det(\underline{P^M}+\underline{C^M})|^2}\times \left[\left|\underline{P^{M-1}I}\right|^2+\left|\underline{P^{M-2}CI}\right|^2+\left|\underline{P^{M-3}C^2I}\right|^2+\cdots+\left|\underline{C^{M-1}I}\right|^2\right], \quad i = 1\ldots M. \tag{35}$$

The injected noise is assumed to be white with two noise components at $\omega_0 - \omega_m$ and $\omega_0 + \omega_m$. The noise power spectral density of each component is $S_n(\omega_m) = i_n^2/2 = 4kT/R$. Hence, the single side band phase noise expressions at the nodes of the ith oscillator can be given as

$$\begin{aligned}[\mathcal{L}(\omega_m)]_{N\times 1} &= \frac{S_\theta(\omega_m)}{2} \\ &= \frac{8kT}{R}\frac{(a^2+b^2)}{I_{osc}^2 b^4}\frac{1}{|\det(\underline{P^M}+\underline{C^M})|^2}\times \\ &\left[\left|\underline{P^{M-1}I}\right|^2+\left|\underline{P^{M-2}CI}\right|^2+\left|\underline{P^{M-3}C^2I}\right|^2+\cdots+\left|\underline{C^{M-1}I}\right|^2\right] \\ & i = 1\ldots M\end{aligned} \tag{36}$$

where $S_\theta(\omega_m)$ is the phase power spectral density.

ACKNOWLEDGMENT

The authors would like to thank UMC for chip fabrication and TI for partial funding. They also thank M. El-Nozahi, M. Elsayed, and E. Pankratz for their help and valuable discussions.

REFERENCES

[1] B. Razavi, "Design considerations for direct-conversion receivers," *IEEE Trans. Circuits Syst. II, Analog Digit. Signal Process*, vol. 44, no. 6, pp. 428–435, Jun. 1997.

[2] L. Wu and W. C. Black Jr., "A low-jitter skew-calibrated multi-phase clock generator for time-interleaved applications," *IEEE ISSCC Dig. Tech. Papers*, pp. 396–397, Feb. 2001.

[3] P. Liao and R. A. York, "A new phase-shifterless beam scanning technique using arrays of coupled oscillators," *IEEE Trans. Microwave Theory Tech.*, vol. 41, pp. 1810–1815, Oct. 1993.

[4] H.-C. Chang, X. Cao, U. K. Mishra, and R. A. York, "Phase noise in coupled oscillators: Theory and experiment," *IEEE Trans. Microwave Theory Tech.*, vol. 45, no. 5, pp. 604–615, May 1997.

[5] L. Romano, S. Levantino, C. Samori, and A. L. Lacaita, "Multiphase LC oscillators," *IEEE Trans. Circuits Syst. I: Regular Papers*, vol. 53, no. 7, pp. 1579–1588, Jul. 2006.

[6] A. Mirzaei, M. E. Heidari, R. Bagheri, S. Chehrazi, and A. A. Abidi, "The quadrature LC oscillator: A complete portrait based on injection locking," *IEEE J. Solid-State Circuits*, vol. 42, no. 9, pp. 1916–1932, Sep. 2007.

[7] J. Van Der Tang, D. Kasperkovitz, and A. H. M. van Roermund*, High-Frequency Oscillator Design for Integrated Transceivers*. Dordrecht, The Netherlands: Kluwer Academic Publishers, 2003.

[8] J. J. Kim and B. Kim, "A low-phase-noise CMOS LC oscillator with a ring structure," *IEEE ISSCC Dig. Tech. Papers*, pp. 430–431, Feb. 2000.

[9] J. G. Maneatis and M. A. Horowitz, "Precise delay generation using coupled oscillators," *IEEE J. Solid-State Circuits*, vol. 28, no. 12, pp. 1273–1282, Dec. 1993.

[10] S.-C. Yen and T.-H. Chu, "An Nth-harmonic oscillator using an N-push coupled oscillator array with voltage-clamping circuits," *IEEE IMS Dig. Tech. Papers*, vol. 3, pp. 2169–2172, Jun. 2003.

[11] M. M. Abdul-Latif and E. Sánchez-Sinencio, "A 3.16–12.8 GHz low phase noise N-push/M-push cyclic coupled ring oscillator," in *IEEE RFIC Symp. Dig.*, Jun. 2011, pp. 405–408.

[12] A. Mirzaei, M. E. Heidari, R. Bagheri, and A. A. Abidi, "Multi-phase injection widens lock range of ring-oscillator-based frequency dividers," *IEEE J. Solid-State Circuits*, vol. 43, no. 3, pp. 656–671, Mar. 2008.

[13] R. A. York, "Nonlinear analysis of phase relationships in quasi-optical oscillator arrays," *IEEE Trans. Microwave Theory Tech.*, vol. 41, no. 10, pp. 1799–1809, Oct. 1993.

[14] S. Li, I. Kipnis, and M. Ismail, "A 10-GHz CMOS quadrature LC-VCO for multirate optical applications," *IEEE J. Solid-State Circuits*, vol. 38, no. 10, pp. 1626–1634, Oct. 2003.

[15] D. K. Shaeffer and S. Kudszus, "Performance-optimized microstrip coupled VCOs for 40-GHz and 43-GHz OC-768 optical transmission," *IEEE J. Solid-State Circuits*, vol. 38, no. 7, pp. 1130–1138, Jul. 2003.

[16] Y.-L. Tang and H. Wang, "Triple-push oscillator approach: Theory and experiments," *IEEE J. Solid-State Circuits*, vol. 36, no. 10, pp. 1472–1479, Oct. 2001.

[17] B. Catli and M. M. Hella, "Triple-push operation for combined oscillation/divison functionality in millimeter-wave frequency synthesizers," *IEEE J. Solid-State Circuits*, vol. 45, no. 8, pp. 1575–1589, Aug. 2010.

[18] C.-C. Li, C.-C. Chen, B.-J. Huang, P.-C. Huang, K.-Y. Lin, and H. Wang, "A novel ring-based triple-push 0.2-to-34 GHz VCO in 0.13 μm CMOS technology," *IEEE IMS Dig. Tech. Papers*, pp. 347–350, Jun. 2008.

[19] L. Dai and R. Harjani, "Design of low-phase-noise CMOS ring oscillators," *IEEE Trans. Circuits Syst. II, Analog Digit. Signal Process*, vol. 49, no. 5, pp. 328–338, May 2002.

[20] T. Lee*, The Design of CMOS Radio Frequency Integrated Circuits*. Cambridge, U.K.: Cambridge Univ. Press, 1998.

$$\underline{P} = \begin{bmatrix} X+kY+j\omega_m RC & 0 & \cdots & 0 & -X \\ -X & X+kY+j\omega_m RC & 0 & \cdots & 0 \\ 0 & -X & \ddots & \ddots & \vdots \\ \vdots & \ddots & \ddots & \ddots & 0 \\ 0 & \cdots & 0 & -X & X+kY+j\omega_m RC \end{bmatrix}_{NxN} \tag{33}$$

[21] A. Abidi, “Phase noise and jitter in CMOS ring oscillators,” *IEEE J. Solid-State Circuits*, vol. 41, no. 8, pp. 1803–1816, Aug. 2006.

[22] Y. Ito, H. Sugawara, K. Okada, and K. Masu, “A 0.98 to 6.6 GHz tunable wideband VCO in a 180 nm CMOS technology for reconfigurable radio transceiver,” *ASSCC Dig. Tech. Papers*, pp. 359–362, Nov. 2006.

[23] B. Fahs, W. Y. Ali-Ahmad, and P. Gamand, “A two-stage ring oscillator in 0.13-μm CMOS for UWB impulse radio,” *IEEE Trans. Microwave Theory Tech.*, vol. 57, no. 5, pp. 1074–1082, May 2009.

[24] A. Rezayee and K. Martin, “A coupled two-stage ring oscillator,” in *Proc. IEEE Midwest Circuits Syst. Symp.*, Aug. 2001, pp. 878–881.

[25] A. Rezayee and K. Martin, “A 10-Gb/s clock recovery circuit with linear phase detector and coupled two-stage ring oscillator,” in *Proc. Eur. Solid-State Circuits Conf. (ESSCIRC)*, Sep. 2002, pp. 419–422.

[26] C. Li and J. Lin, “A 1–9 GHz linear-wide-tuning-range quadrature ring oscillator in 130 nm CMOS for non-contact vital sign radar application,” *IEEE Microw. Wireless Compon. Lett.*, vol. 20, no. 1, pp. 34–36, Jan. 2010.

[27] E. Tatschl-Unterberger, S. Cyrusian, and M. Ruegg, “A 2.5 GHz phase-switching PLL using a supply controlled 2-delay-stage 10 GHz ring oscillator for improved jitter/mismatch,” in *Proc. IEEE Int. Circuits Syst. Symp.*, May 2005, pp. 5453–5456.

[28] V. De Heyn *et al.*, “A fast start-up 3 GHz-10 GHz digitally controlled oscillator for UWB impulse radio in 90 nm CMOS,” in *Proc. Eur. Solid-State Circuits Conf. (ESSCIRC)*, Sep. 2007, pp. 484–487.

[29] L. Cai and R. Harjani, “1–10 GHz inductorless receiver in 0.13 μm CMOS,” in *IEEE RFIC Symp. Dig.*, Jun. 2009, pp. 61–64.

[30] W.-M. L. Kuo, J. D. Cressler, Y.-J. E. Chen, and A. J. Joseph, “An inductorless Ka-band SiGe HBT ring oscillator,” *IEEE Microw. Wireless Compon. Lett.*, vol. 15, no. 10, pp. 682–684, Oct. 2005.

[31] N. Saniei, H. Djahanshahi, and C. A. T. Salama, “25 GHz inductorless VCO in a 45 GHz SiGe technology,” in *IEEE RFIC Symp. Dig.*, May 2003, pp. 269–272.

[32] W.-M. L. Kuo, J. D. Cressler, Y.-J. E. Chen, and A. J. Joseph, “A compact 21 GHz inductorless differential quadrature ring oscillator implemented in SiGe HBT technology,” *Mater. Sci. Semicond. Process.*, vol. 8, pp. 445–449, Feb. 2005.

[33] H. Djahanshahi, N. Saniei, S. P. Voinigescu, M. C. Maliepaard, and C. A. T. Salama, “A 20-GHz InP-HBT voltage-controlled oscillator with wide frequency tuning range,” *IEEE Trans. Microw. Theory Tech.*, vol. 49, no. 9, pp. 1566–1572, Sep. 2001.

[34] C.-C. Chen, C.-C. Li, B.-J. Huang, K.-Y. Lin, H.-W. Tsao, and H. Wang, “Ring-based triple-push VCOs with wide continuous tuning ranges,” *IEEE Trans. Microwave Theory Tech.*, vol. 57, no. 9, pp. 2173–2183, Sep. 2009.

[35] R. M. Kodkani and L. E. Larson, “A 25 GHz quadrature voltage controlled ring oscillator in 0.12 μm SiGe HBT,” in *Silicon Monolithic Integrated Circuits in RF Systems Topical Meeting Dig.*, 2006, pp. 18–20.

Mohammed M. Abdul-Latif (S’03) received the B.Sc. and M.Sc. degrees, both in electrical engineering, from Cairo University, Cairo, Egypt, in 2002 and 2005, respectively, and the Ph.D. degree from Texas A&M University, College Station, TX, in 2011.

From 2002 to 2005, he was a teaching and research assistant with the Electronics and Communications Engineering Department, Cairo University. From 2005 to 2011, he was a research assistant with the Analog and Mixed Signal Center at Texas A&M University. In 2008, he was an intern with Texas Instrument Incorporated, Dallas, TX. He is currently a Staff Scientist with Broadcom Corporation, Irvine, CA. His research interests include high speed mixed-signal circuits, frequency synthesizers and oscillator circuit design.

Dr. Abdul-Latif is the recipient of the Motorola Fellowship (2005–2008), Texas Instruments Excellence Fellowship (2010–2011), and the Cary N. Smith ’34 Academic Excellence Award for 2010/2011.

Edgar Sánchez-Sinencio (F’92–LF’09) was born in Mexico City, Mexico. He received the degree in communications and electronic engineering (Professional degree) from the National Polytechnic Institute of Mexico, Mexico City, the M.S.E.E. degree from Stanford University, Stanford, CA, and the Ph.D. degree from the University of Illinois at Champaign-Urbana in 1966, 1970, and 1973, respectively.

His research work has more than 3,200 citations according to the Thomson Reuters Scientific Citation Index. He has graduated 47 M.Sc. and 37 Ph.D. students. He is a co-author of six books on different topics, such as RF circuits, low-voltage low-power analog circuits, and neural networks. He is currently the TI J. Kilby Chair Professor and Director of the Analog and Mixed-Signal Center at Texas A&M University. His current interests are in the area of power management, analog and medical electronics circuit design.

Dr. Sánchez-Sinencio is a former Editor-in-Chief of IEEE TRANSACTIONS ON CIRCUITS AND SYSTEMS II and a former IEEE CAS Vice President-Publications. In November 1995 he was awarded an Honoris Causa Doctorate by the National Institute for Astrophysics, Optics and Electronics, Mexico. This degree was the first honorary degree awarded for microelectronic circuit-design contributions. He is a co-recipient of the 1995 Guillemin-Cauer Award for his work on cellular networks. He was also the co-recipient of the 1997 Darlington Award for his work on high-frequency filters. He received the IEEE Circuits and Systems Society Golden Jubilee Medal in 1999. He is the recipient of the prestigious IEEE Circuits and Systems Society 2008 Technical Achievement Award. He was the IEEE Circuits and Systems Society’s Representative to the IEEE Solid-State Circuits Society during 2000–2002. He was a member of the IEEE Solid-State Circuits Society Fellow Award Committee from 2002 to 2004. He has received the Texas Senate Proclamation #373 for Outstanding Accomplishments in 1996. His website can be found at: http://amesp02.tamu.edu/~sanchez.